ACSNANO

www.acsnano.org

ARTICLE

Synthesis and Formation Mechanism of Colloidal Janus-Type $Cu_{2-x}S/CuInS_2$ Heteronanorods *via* Seeded Injection

Chenghui Xia,[⊥] Christina H. M. van Oversteeg,[⊥] Veerle C. L. Bogaards, Tim H. M. Spanjersberg, Nienke L. Visser, Anne C. Berends, Johannes D. Meeldijk, Petra E. de Jongh, and Celso de Mello Donega*

Cite This: *ACS Nano* 2021, 15, 9987–9999

Read Online

ACCESS | Metrics & More | Article Recommendations | Supporting Information

ABSTRACT: **Colloidal heteronanocrystals allow for the synergistic combination of properties of different materials. For example, spatial separation of the photogenerated electron and hole can be achieved by coupling different semiconductors with suitable band offsets in one single nanocrystal, which is beneficial for improving the efficiency of photocatalysts and photovoltaic devices. From this perspective, axially segmented semiconductor heteronanorods with a type-II band alignment are particularly attractive since they ensure the accessibility of both photogenerated charge carriers. Here, a two-step synthesis route to $Cu_{2-x}S/CuInS_2$ Janus-type heteronanorods is presented. The heteronanorods are formed by injection of a solution of preformed $Cu_{2-x}S$ seed nanocrystals in 1-dodecanethiol into a solution of indium oleate in oleic acid at 240 °C. By varying the reaction time, Janus-type heteronanocrystals with different sizes, shapes, and compositions are obtained. A mechanism for the formation of the heteronanocrystals is proposed. The first step of this mechanism consists of a thiolate-mediated topotactic, partial Cu^+ for In^{3+} cation exchange that converts one of the facets of the seed nanocrystals into $CuInS_2$. This is followed by homoepitaxial anisotropic growth of wurtzite $CuInS_2$. The $Cu_{2-x}S$ seed nanocrystals also act as sacrificial Cu^+ sources, and therefore, single composition $CuInS_2$ nanorods are eventually obtained if the reaction is allowed to proceed to completion. The two-stage seeded growth method developed in this work contributes to the rational synthesis of $Cu_{2-x}S/CuInS_2$ heteronanocrystals with targeted architectures by allowing one to exploit the size and faceting of premade $Cu_{2-x}S$ seed nanocrystals to direct the growth of the $CuInS_2$ segment.**

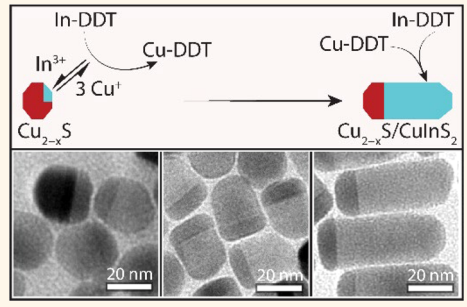

KEYWORDS: *copper indium sulfide, Janus-type heteronanorod, cation exchange, epitaxial growth, copper(I) sulfide, seeded growth*

Colloidal nanocrystals (NCs) are attractive materials for various applications as they have size- and shape-dependent properties.[1−4] The interesting properties of these nanomaterials can be further extended by the use of heteronanocrystals (HNCs), where two (or more) different materials are combined into one NC through one or more heterointerfaces.[1−4] In this way, the optical, magnetic, or catalytic properties of different materials can be synergistically combined. In addition, novel properties can arise and be tailored by the size, shape, and composition of each part of the HNC and by the way in which the different segments are connected.[1−4]

The optoelectronic properties of semiconductor HNCs are determined by the bandgap and band alignment of the materials comprising the HNC. Depending on the band alignment of the materials at the heterointerface, different charge carrier localization regimes can be distinguished, namely type-I, type-I$^{1/2}$ (or *quasi*-type-II), and type-II,[2,4] whereas in a type-I HNC the photogenerated charge carriers are confined in the same part of the HNC; in a type-II HNC they are spatially separated on different sides of the heterojunction. This spatial separation of the exciton leads to longer exciton lifetimes and is interesting for many applications, such as photovoltaics and photocatalysis.[4−8] The band offset is thus an important parameter in the design of HNCs and can be tailored by the composition and size of each component of the HNC. The architecture of the HNC is

Received: February 18, 2021
Accepted: June 8, 2021
Published: June 10, 2021

crucial, as it determines the accessibility of the photogenerated charge carriers at the particle surface.[4] For example, morphologies such as axially segmented Janus-type heteronanorods or dumbbell nanorods are most suitable for photovoltaic and photocatalytic applications[5−8] since they make both photogenerated charge carriers accessible.[1−4]

Several semiconductor HNCs with type-I$^{1/2}$ and type-II band alignments, including CdSe/CdS and ZnSe/CdS dot-in-rod HNCs,[9−12] ZnSe/CdS/ZnSe dumbbell nanorods,[13] and CdSe/CdS/ZnS double heterojunction nanorods,[14] have been shown to exhibit improved charge carrier separation. Moreover, type-II CdS/PbS heteronanorods have been shown to behave as nanoscale *p-n* heterojunctions.[15] However, the applicability of HNCs based on Cd and Pb is severely limited by the toxicity of these elements, and hence, alternative compositions that are more environmentally benign are needed.[16,17] $Cu_{2-x}S$ is an attractive candidate because of its relatively low cost and low toxicity.[16] In addition, the bandgap of $Cu_{2-x}S$, ranging from 1.1 eV for Cu_2S to 2.0 eV for CuS,[16] makes it an interesting material for photovoltaic and photocatalytic applications. $CuInS_2$ is a suitable second component for $Cu_{2-x}S$-based HNCs due to its similar crystal structure and bulk band offsets that can lead to type-I$^{1/2}$ carrier localization (*viz.* band gap: 1.5 eV, valence band offset: 0.4 eV and negligible conduction band offset with respect to Cu_2S).[18−20] Additionally, $Cu_{2-x}S$ is a *p*-type semiconductor, while $CuInS_2$ is often *n*-type doped due to native defects.[21−24] Hence, an interparticle *p*−*n* heterojunction can be formed between the two materials, thereby improving the exciton dissociation and spatial separation of the photogenerated electron and hole.[4−8] However, to allow harnessing of the spatially separated charge carriers, strict control over the size, shape, heteroarchitecture, and heterointerface of the $Cu_{2-x}S$/$CuInS_2$ HNCs is crucial.

Copper chalcogenide-based HNCs with different compositions (*viz.* $Cu_{2-x}S$/ZnS,[25−30] $Cu_{2-x}S$/MnS,[31] $Cu_{2-x}S$/CdS,[32] $Cu_{2-x}S$/PbS,[33] $Cu_{2-x}S$/In_2S_3,[34,35] $Cu_{2-x}S$/$CuInS_2$,[36−46] $CuInS_2$/ZnS,[47,48] $CuInSe_2$/$CuInS_2$[49]) have been obtained by several synthetic strategies, but the degree of control over these nanomaterials is still lagging behind that achieved for the prototypical Cd- and Pb-containing HNCs, despite many important advances in recent years. Owing to the high mobility and low-charge of Cu^+, postsynthetic cation exchange reactions have been extensively used to successfully obtain a variety of copper chalcogenide-based (H)NCs.[16,50−52] In particular, $Cu_{2-x}S$/$CuInS_2$ HNCs with various architectures have been synthesized, such as $Cu_{2-x}S$@$CuInS_2$ heteronanodisks[42,43] and axially segmented $Cu_{2-x}S$/$CuInS_2$ heteronanorods.[44,46] The recent work by Schaak and co-workers[53] is particularly relevant, as the authors demonstrated a multistep sequential cation-exchange synthesis strategy through which 20 nm diameter $Cu_{1.8}S$ nanorods were converted into 113 distinct multicomponent axially segmented heteronanorods, with up to eight segments, made of up to six materials ($Cu_{2-x}S$, ZnS, $CuInS_2$, $CuGaS_2$, CoS, CdS). Nevertheless, the synthesis of Janus-type $Cu_{2-x}S$/$CuInS_2$ heteronanorods by partial Cu^+ for In^{3+} cation exchange is particularly challenging due to the low energy barriers for Cu^+−In^{3+} interdiffusion, the high miscibility of $Cu_{2-x}S$ and In_yS_z phases, and the pronounced tolerance of nanoscale copper indium sulfide to stoichiometry deviations,[16,50] which often favor the conversion of the $Cu_{2-x}S$ template NCs into homogeneous $Cu_xIn_yS_2$ NCs rather than HNCs.[16,30,49−52,54] Additionally, even when suitable conditions are identified to induce the formation of heteroNCs,[42−44,53] it remains difficult to precisely control the location of the $CuInS_2$ segment since the cation exchange may start simultaneously at different points, yielding distinct heterostructured NCs within the same sample (*e.g.*, single-tip $Cu_{2-x}S$/$CuInS_2$ and central band $Cu_{2-x}S$/$CuInS_2$/$Cu_{2-x}S$ heteronanorods).[53]

To date, the most extensively used approach to synthesize Janus-type anisotropic $Cu_{2-x}S$/$CuInS_2$ HNCs is a one-pot synthesis method in which all precursors are added in one reaction flask and subsequently heated to the reaction temperature.[36−41,45] The formation of the $Cu_{2-x}S$/$CuInS_2$ HNCs has been shown to occur through sequential discrete steps, of which the first is the nucleation and growth of $Cu_{2-x}S$ NCs. This is followed by anisotropic growth of $CuInS_2$ onto the *in situ* formed $Cu_{2-x}S$ seed NCs. If the reaction is allowed to proceed to completion, the HNCs are eventually converted to single-component wurtzite $CuInS_2$ nanorods.[36−41,45] A one-pot approach is appealing due to its simplicity, but the balance between the precursor reactivities is challenging, offering limited control over the reaction kinetics. The quality (size, shape, composition, heterointerfaces) of the product $Cu_{2-x}S$/$CuInS_2$ HNCs strongly depends on the first step (i.e., nucleation and growth of the $Cu_{2-x}S$ seed NCs), which is, however, difficult to control since it takes place under strongly changing physical−chemical conditions.

To improve the control over the synthesis of Janus-type $Cu_{2-x}S$/$CuInS_2$ heteronanorods, while gaining a deeper understanding of their formation mechanism, we investigated in this work a two-step seeded-growth approach. Multistage seeded injection synthesis strategies are highly versatile and have been successfully used to obtain Cd-chalcogenide based-HNCs of various heteroarchitectures.[9−13,55−57] This approach has recently been extended to Cu-chalcogenide based-HNCs, such as $Cu_{2-x}S$/MS (M = Zn, Cd, Mn) HNCs,[30,58] $CuInS_2$/ZnS core/shell and dot-in-rod HNCs,[47,48] and $CuInS_2$/CdS tetrapod HNCs.[59,60] The most important advantage of the multistage seeded injection approach over the one-pot approach is that radically different physical−chemical conditions can be used to synthesize the seed NCs and the HNCs grown from them.[1,4] This allows for a much tighter control over the outcome of the synthesis since the impact of competing processes can be minimized by using conditions that favor heteroepitaxial growth and the characteristics of the preformed seed NCs (composition, size, shape, crystal structure, faceting, surface chemistry) can be tailored with more precision and versatility.[1,4]

The use of the multistage seeded-injection strategy allowed us to separate and independently optimize the two stages identified in the one-pot synthesis of $Cu_{2-x}S$/$CuInS_2$ HNCs. First, well-defined low-chalcocite $Cu_{2-x}S$ hexagonal nanoplatelets with a diameter of 24.1 ± 1.2 nm and a thickness of 17.4 ± 0.9 nm were synthesized and isolated. In a second step, these preformed $Cu_{2-x}S$ seed NCs were suspended in 1-dodecanethiol (DDT) and injected into a hot indium oleate solution. Our results show that the first step in the formation of the $Cu_{2-x}S$/$CuInS_2$ HNCs is a thiolate-mediated topotactic, partial Cu^+ for In^{3+} exchange that converts one of the facets of the $Cu_{2-x}S$ seed NCs into $CuInS_2$. Once the $CuInS_2$ surface forms, the cation-exchange reaction is overtaken by homoepitaxial anisotropic growth of wurtzite $CuInS_2$. The Cu^+ for the growth of $CuInS_2$ is provided by the $Cu_{2-x}S$ seed NCs, which slows the overall growth rate, leading to a good control

https://doi.org/10.1021/acsnano.1c01488
ACS Nano 2021, 15, 9987−9999

over the size, shape, and composition of product Janus-type $Cu_{2-x}S/CuInS_2$ HNCs. The mechanistic insights gained in this work will enable further optimization of the synthesis strategy proposed here since they show that its outcome is determined by a competition between cation exchange and epitaxial growth. These two processes depend differently on physical−chemical variables (*e.g.*, temperature, adjuvant ligands, *etc.*)[1,4,16,47,50−53] and can be independently modulated. The two-stage seeded-injection synthesis strategy developed here thus contributes toward the rational synthesis of $Cu_{2-x}S/CuInS_2$ HNCs by allowing one to take advantage of the wealth of knowledge available on seeded-injection[1,4,30,47,48,55−58,61] and cation-exchange[16,30,47−53] synthesis protocols and the high degree of control already achieved over the size, shape, and crystal structure of $Cu_{2-x}S$ NCs[16,30,54,62−73] to tailor the $CuInS_2$ segment and the $Cu_{2-x}S/CuInS_2$ heterointerface.

RESULTS AND DISCUSSION

This section is organized as follows. In the first subsection, we address control experiments in which $Cu_{2-x}S/CuInS_2$ HNCs were prepared by a one-pot approach under conditions that are fully comparable to the two-stage seeded-injection approach developed in our work. Subsequently, we focus on the synthesis and characterization of the $Cu_{2-x}S$ NCs that were used as seeds. We then proceed with a subsection on the $Cu_{2-x}S/CuInS_2$ HNCs prepared by the two-stage seeded-injection approach. In the final subsection, we propose a formation mechanism for $Cu_{2-x}S/CuInS_2$ HNCs by seeded-injection.

$Cu_{2-x}S/CuInS_2$ HNCs Prepared by One-Pot Direct Synthesis. $Cu_{2-x}S/CuInS_2$ HNCs have been previously obtained by one-pot synthesis approaches.[36−38,40,41] In order to compare the two-stage seeded injection approach developed in our work to these previous reports, we performed a control one-pot direct synthesis in which a mixture of copper(I) acetate in 1-DDT was injected into a preheated mixture of indium oleate in oleic acid at 240 °C (see the Methods for details). These conditions are identical to those used in the two-stage seeded injection approach discussed below (see the Methods for details), except that Cu(I) is added as copper acetate instead of $Cu_{2-x}S$ seed NCs. The reaction temperature is the same previously used in one-pot synthesis approaches,[37,40] but the chemical complexity of the reaction system has been reduced by using only two coordinating solvents: 1-DDT (which acts also as sulfur-source) and oleic acid. Previous works used a combination of *t*-DDT and 1-DDT under the assumption that the lower thermal stability of *t*-DDT would make it the preferred S-source, while the more stable 1-DDT would act only as ligand.[37,40] However, this is an unnecessary kinetic complication since it is well-known that 1-DDT can act as solvent, S-source, and ligand in the synthesis of $Cu_{2-x}S$ and $CuInS_2$ NCs (see also the next section).[16,47,66,67] Further, mixtures of oleic acid, trioctylphosphine oxide, and oleylamine have been used as coordinating solvents (in addition to DDT).[37,40] As will be demonstrated below, high-quality anisotropic $Cu_{2-x}S/CuInS_2$ HNCs can be obtained by the multistage seeded injection approach in the absence of the latter two ligands, which are thus left out for the sake of simplicity. Oleic acid was kept as the coordinating solvent since it is necessary to obtain a sufficiently stable In^{3+} precursor (In oleate). Another relevant difference between the control one-pot synthesis carried out in the present work and those previously reported in the literature is that in the present case a hot-injection approach is used (*i.e.*, Cu(I) acetate and 1-DDT are injected together in an indium oleate solution at 240 °C), while previous reports used a heat-up approach (*i.e.*, a solution containing Cu(I) and In(III) is heated to 240 °C and DDT is injected into it before the final reaction temperature has been reached).[36−38,40]

Transmission electron microscopy (TEM) images of samples collected at different reaction times are shown in the Supporting Information (Figure S1). $Cu_{2-x}S$ NCs are formed at the early stages of the reaction (<2 min) due to their lower activation energy for nucleation and evolve into $Cu_{2-x}S/CuInS_2$ HNCs as the reaction progresses. Bottle-shaped $Cu_{2-x}S/CuInS_2$ HNCs are already present after 3 min of reaction, as evidenced by the interparticle contrast observed in the TEM image, and coexist with $Cu_{2-x}S$ NCs (Figure S1a). As the reaction proceeds, the fraction of HNCs becomes increasingly larger until single composition $Cu_{2-x}S$ NCs are no longer observed (Figure S1, 5 min). Concomitantly, the $CuInS_2$ segment of the HNCs grows increasingly longer, while the $Cu_{2-x}S$ segment shrinks (Figure S1, 5−30 min). At sufficiently long times (>60 min), the sharp interparticle contrast is no longer observed, indicating that the reaction product consists of homogeneous double-tapered anisotropic $CuInS_2$ NCs with a large polydispersity in size and shape (Figure S1, 90 min). These results are similar to those previously reported for one-pot heat-up synthesis approaches,[36−38,40,41] implying that the outcome of the reaction is primarily dictated by the nucleation and growth kinetics of the $Cu_{2-x}S$ NCs, which appear to be largely insensitive to the heating protocol used (*i.e.*, heat-up or hot-injection). This is consistent with the formation mechanism of $Cu_{2-x}S$ NCs from Cu(I) thiolates in which the rate-limiting step is the thermally induced cleavage of the C−S bond of the DDT molecules coordinated to the Cu (I) ions,[74] leading to slow, reaction-limited nucleation rates. This explains the large size and shape polydispersity of the product $Cu_{2-x}S/CuInS_2$ HNCs and $CuInS_2$ NCs since the formation of the $Cu_{2-x}S$ NCs that act as seeds is spread over a wide time interval and is followed by a fast growth process under changing physical−chemical conditions. As will be shown below, a two-stage seeded-injection approach provides a better control over the formation and growth of the $CuInS_2$ segment, thereby improving the quality of the $Cu_{2-x}S/CuInS_2$ heterointerface and the size and shape dispersion of the HNCs. To this end, high-quality $Cu_{2-x}S$ seed NCs must first be prepared.

Synthesis and Structural Characterization of $Cu_{2-x}S$ Seed NCs. Figure 1a shows a high-resolution TEM (HRTEM) image of the $Cu_{2-x}S$ NCs used as seeds in the multistage seeded-injection approach (see the Methods for details). The $Cu_{2-x}S$ NCs are hexagonal nanoplatelets and have a diameter of 24.1 ± 1.2 nm and a thickness of 17.4 ± 0.9 nm. Fourier transform (FT) analyses demonstrate that these NCs have the monoclinic low-chalcocite crystal structure (Figure 1a). In the seeded-injection synthesis approach developed in this work, the $Cu_{2-x}S$ seed NCs are injected into an indium oleate solution at 240 °C (see the Methods for details). For bulk $Cu_{2-x}S$, it is known that the low-chalcocite structure can readily undergo a phase transition to the hexagonal high-chalcocite at high temperatures.[75−77] The two phases have similar hexagonal close packing of sulfur ions but differ with respect to the distribution of the Cu atoms.[75] To verify whether phase transformation of the $Cu_{2-x}S$ seed NCs from low chalcocite to high chalcocite occurs after the

https://doi.org/10.1021/acsnano.1c01488
ACS Nano 2021, 15, 9987−9999

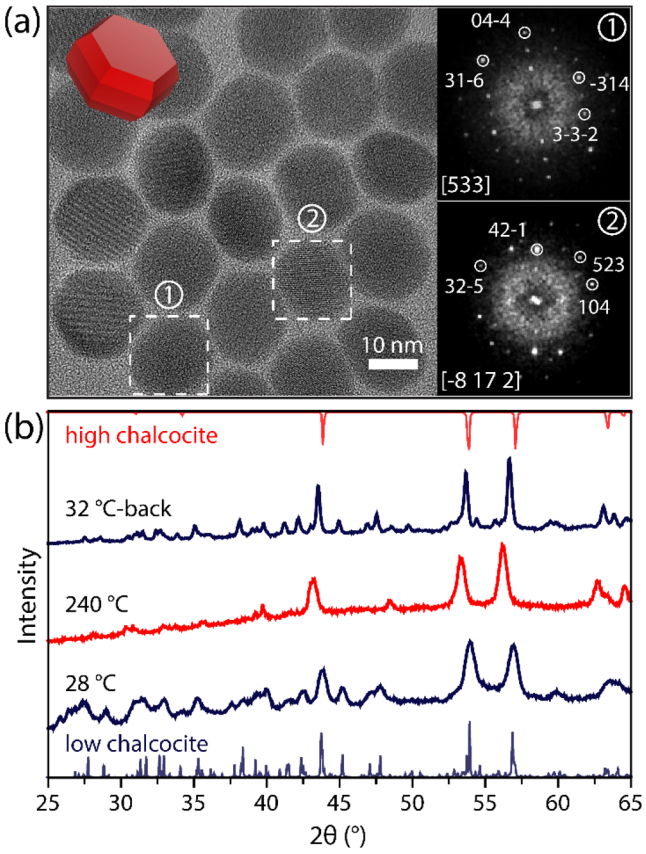

Figure 1. (a) HRTEM images of $Cu_{2-x}S$ seed NCs. Panels 1 and 2 are the FT patterns of the $Cu_{2-x}S$ NCs marked by white squares, which are indexed to monoclinic low-chalcocite $Cu_{2-x}S$ viewed along the [533] and [−8 17 2] axis, respectively. Inset: the crystal shape of $Cu_{2-x}S$ seed NCs. (b) *In situ* temperature-dependent XRD patterns of the $Cu_{2-x}S$ seed NCs from 28 to 240 °C and back to 32 °C. The diffraction patterns of low and high chalcocite are very similar but can be distinguished by the additional diffractions observed for low chalcocite at 2θ values of *e.g.*, 45° and 48°, and the range from 25° to 43°.

injection, the crystal structure of the $Cu_{2-x}S$ seed NCs was studied by temperature-dependent X-ray diffraction (XRD) (Figure 1b).

Figure 1b shows the XRD patterns of the $Cu_{2-x}S$ seed NCs at 28 and 240 °C (additional temperatures are shown in Figure S2). The diffractogram shows that at 28 °C the $Cu_{2-x}S$ seed NCs have the monoclinic low-chalcocite phase (PDF Card 00-033-0490), in agreement with the HRTEM analysis (Figure 1a). The diffractogram of the $Cu_{2-x}S$ seed NCs at 240 °C can be indexed to the hexagonal high-chalcocite crystal structure (PDF Card 00-046-1195). After being cooled to room temperature, the $Cu_{2-x}S$ seed NCs return to the monoclinic low-chalcocite phase (Figure 1b and Figure S2), confirming that the reversible temperature-induced phase transition indeed occurs. This process most likely also happens upon injection of the $Cu_{2-x}S$ seed NCs into the indium oleate solution at 240 °C, though the conditions in the reaction flask are different from those during the XRD measurements (i.e., NCs dispersed in a coordinating solvent instead of a dry powder).

$Cu_{2-x}S/CuInS_2$ HNCs by Seeded Injection. To prepare $Cu_{2-x}S/CuInS_2$ HNCs, premade $Cu_{2-x}S$ seed NCs were injected in a hot solution of indium oleate (see Methods for details). All reactions were performed at 240 °C. This temperature was selected for a number of reasons. First, it is the same used in the one-pot control experiment described above and in one-pot experiments reported in the literature.[37,40] Second, this temperature leads to the formation of HNCs at a rate that is sufficiently slow to allow it to be followed in detail (Figure S3, see also discussion below). Lower injection temperatures (200 °C, Figure S3) lead to small tear-shaped NCs, while longer and thinner nanorods are obtained at higher temperatures (260 °C, Figure S3). Most importantly, interparticle contrast is not evident in the NCs obtained at 200 and 260 °C, suggesting that HNCs are not formed at these temperatures. The $Cu_{2-x}S$ NCs discussed above were chosen as seeds because their size and shape are similar to those of the $Cu_{2-x}S$ NCs formed *in situ* at the early stages of the control one-pot synthesis (see above), allowing for a reliable comparison between the two approaches since all other reaction parameters are the same (*viz.*, reaction temperature, composition of the coordinating solvent, nature and concentration of the In^{3+} precursor, total concentration of Cu^+ ions). The only significant difference between the two approaches is that the Cu^+ ions are injected as a solution of Cu(I) acetate in the one-pot approach and as premade $Cu_{2-x}S$ seed NCs in the multistage seeded-injection approach. The chosen seed NCs are also advantageous to our purposes because they are sufficiently large to allow the temporal evolution of the reaction to be followed by TEM, high-angle annular dark field scanning TEM (HAADF-STEM) and energy-dispersive X-ray spectroscopy (EDX). It may be expected that the size, shape, and crystal structure of the seed NCs have a dramatic impact on the outcome of the seeded-injection synthesis.[1,4] However, for the sake of conciseness and clarity, we will focus on just one single type of $Cu_{2-x}S$ seed NCs (*viz.*, low-chalcocite $Cu_{2-x}S$ hexagonal nanoplatelets with diameter of 24.1 ± 1.2 nm and thickness of 17.4 ± 0.9 nm). The exploration of the impact of the size, shape, and crystal structure of the $Cu_{2-x}S$ seed NCs lies beyond the scope of the present work.

By varying the reaction time at 240 °C, heterostructures with different sizes, shapes, and compositions were formed. As will be clear below, the reaction can be divided into three partially overlapping stages: (i) early stage ($t \leq 4$ min), (ii) intermediate stage (4 min $< t \leq 60$ min), and (iii) final stage ($t > 60$ min). In the following, we will sequentially address each of these stages and subsequently proceed with the advanced compositional and structural characterization of HNCs collected at several time points in stage (ii). Figure 2 shows HAADF-STEM images and corresponding EDX elemental maps of samples collected during the first 3 min of reaction after the injection of the $Cu_{2-x}S$ seed NCs (additional images and elemental quantification are provided in Figures S4 and S5, respectively). After 1 min of reaction, the size and shape of the NCs are very similar to those of the original $Cu_{2-x}S$ seed NCs and no indium is observed in the particles (Figure 2a and Figure S4a). After 2 min of reaction, the particle size and shape are still the same, but almost all NCs have an indium-rich area (Figure 2b and Figure S4b). After an additional minute of reaction, the indium-rich area has clearly grown and a well-defined heterointerface is present in the NCs (Figure 2c and Figure S4c). Interestingly, despite these compositional changes, the shape and size of the NCs have not significantly changed. The preserved size and shape combined with the incorporation of indium in the $Cu_{2-x}S$ seed

https://doi.org/10.1021/acsnano.1c01488
ACS Nano 2021, 15, 9987−9999

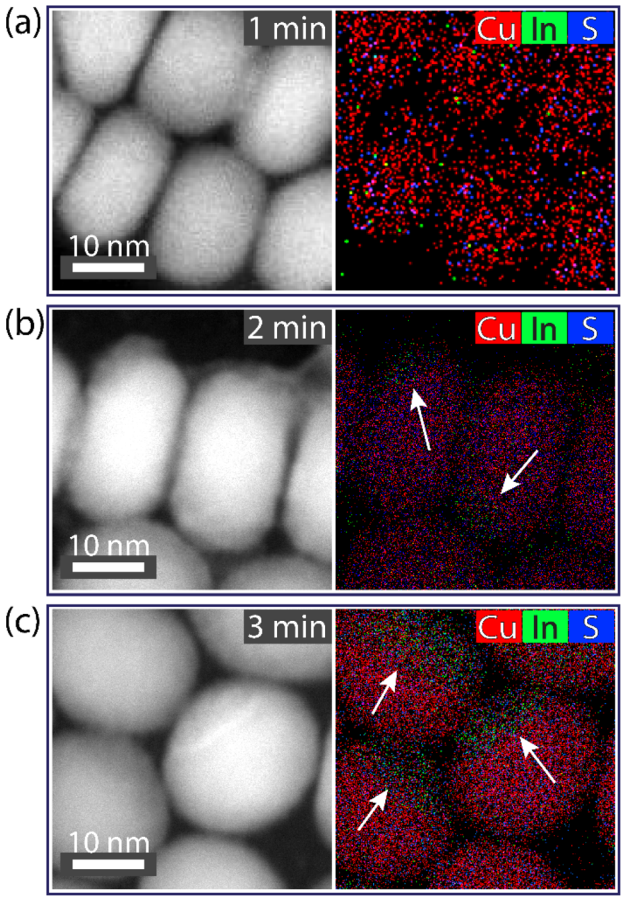

Figure 2. (a–c) HAADF-STEM images and corresponding elemental maps of the $Cu_{2-x}S/CuInS_2$ HNCs formed by the injection of $Cu_{2-x}S$ seed NCs into a solution of indium oleate at 240 °C. Samples after reaction times of (a) 1, (b) 2, and (c) 3 min are shown. After 1 min of reaction, no significant amount of indium was present in the NCs, whereas after 2 and 3 min of reaction indium is clearly incorporated in the $Cu_{2-x}S$ seed NCs and heterointerfaces are formed, as indicated by the white arrows.

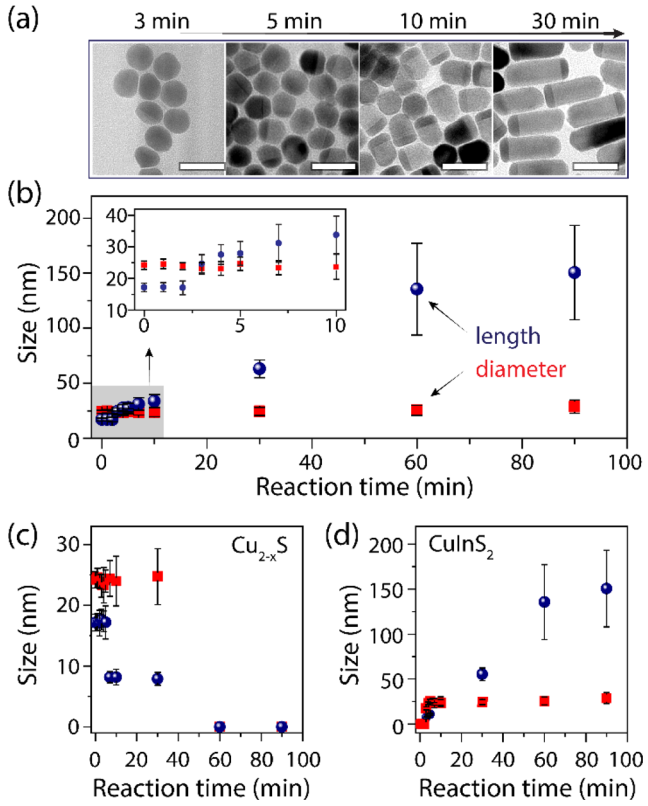

Figure 3. (a) TEM images of $Cu_{2-x}S/CuInS_2$ HNCs formed by the injection of $Cu_{2-x}S$ seed NCs into a solution of indium oleate at 240 °C after reaction times from 3 to 30 min. Scale bars are 50 nm. (b) Average length and diameter of the HNCs obtained at different times after the injection of the $Cu_{2-x}S$ seed NCs. During the first 3 min of reaction, the length of the HNCs remains similar to that of the $Cu_{2-x}S$ seed NCs (shown at time = 0 min), while after 5 min the HNC length starts to increase. The HNC diameter shows no large variation with reaction time. The inset in b is the zoomed-in plot of HNC sizes in the first 10 min. (c, d) The average length (blue spheres) and diameter (red squares) of the $Cu_{2-x}S$ (c) and $CuInS_2$ (d) segments of the product HNCs obtained at different times after the $Cu_{2-x}S$ seed NC injection.

NCs suggests that topotactic partial Cu^+ for In^{3+} cation exchange occurs prior to the epitaxial growth of $CuInS_2$ on the $Cu_{2-x}S$ seed NCs, similar to the observation of $Cu_{1.94}S$–MnS HNCs in the initial stage of a reaction.[31]

With further extension of the reaction time, larger heterostructures are formed. As can be seen in Figure 3a, the size and shape of the NCs start to change 5 min after the injection of the $Cu_{2-x}S$ seed NCs, with the formation of acorn-shaped HNCs and subsequently elongated heteronanorods with sharp heterointerfaces. While the length of the HNCs clearly increases with increasing reaction time, their diameter remains essentially the same (Figure 3b). The pronounced evolution in size and shape of the HNCs shows that after 5 min epitaxial overgrowth of $CuInS_2$ dominates over the initial Cu^+ for In^{3+} cation exchange. The transition from the early stage to the intermediate stage of the reaction is thus marked by the onset of the epitaxial overgrowth of $CuInS_2$. Moreover, the diameter of the $Cu_{2-x}S$ segments of the HNCs remains constant while their length continuously decreases during the reaction until they completely disappear (Figure 3c). In contrast, the length of the $CuInS_2$ segments gradually increases with a nearly constant diameter (Figure 3d). These observations suggest that the growth of $CuInS_2$ likely occurs at the expense of the $Cu_{2-x}S$ seed NCs. The size and shape of the particles do not significantly change after 60 min of reaction (Figure 3b), but the sharp heterointerfaces are no longer observed, indicating that the NCs have a uniform composition (Figure S6). The final stage of the reaction is thus marked by the disappearance of the $Cu_{2-x}S$ tips. Further changes to the product $CuInS_2$ NCs will then only occur by slow growth (up to ~90 min, Figure 3c,d) and ripening.

To investigate the origin of the contrast observed in the TEM images discussed above, HAADF-STEM combined with EDX was employed. Figure 4 shows two-dimensional elemental maps of samples collected after reaction times of 10 and 30 min. The elemental maps show that the tips of the particles contain no indium, whereas copper and sulfur are present in the whole NC. Sulfur is uniformly distributed over the whole particle and copper is most abundant in the tips. The chemical composition of the HNCs obtained from the elemental maps and from bulk EDX spectra is summarized in Figures S7 and S8. Both samples consist of a short $Cu_{2-x}S$ tip attached to a $CuInS_2$ segment, which grows longer with reaction time. The amount of In in the $Cu_{2-x}S$ tips is negligible, being similar to the background In concentration

https://doi.org/10.1021/acsnano.1c01488
ACS Nano 2021, 15, 9987–9999

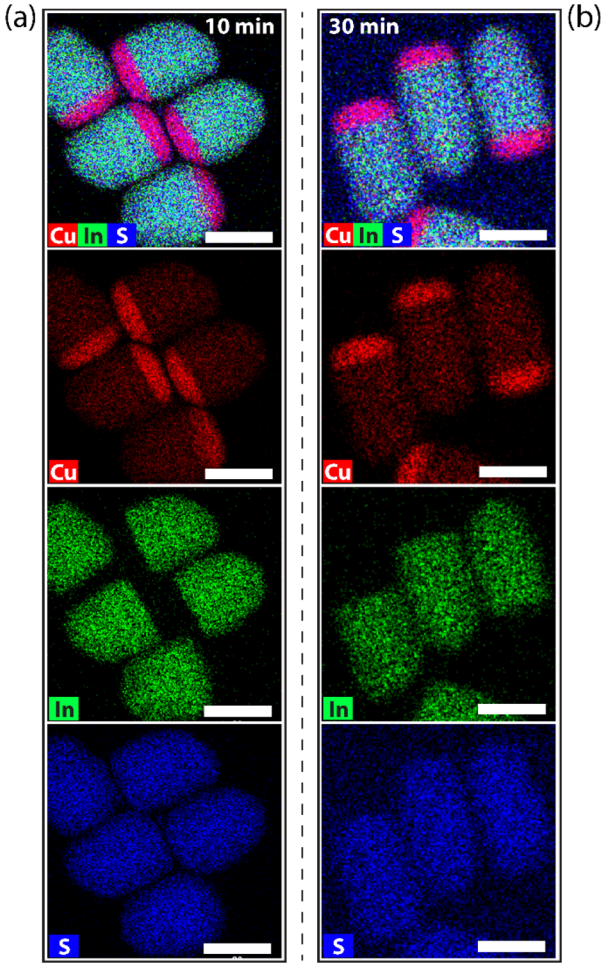

Figure 4. (a,b) Elemental maps of $Cu_{2-x}S/CuInS_2$ HNCs formed by injection of $Cu_{2-x}S$ seed NCs into a solution of indium oleate at 240 °C after reaction times of 10 min (a) and 30 min (b). Scale bars are 20 nm.

which likely originates from unwashed In oleate and/or In thiolate (Figure S7). As discussed above (Figure 3c,d), the volume of the $CuInS_2$ segment significantly increases from 10 to 30 min, while that of the $Cu_{2-x}S$ tip remains essentially constant. After another 10 min of reaction, the aspect ratio of the HNCs has increased to ~4, while the volume of the $Cu_{2-x}S$ tips is reduced by ~20%. This corroborates the observations discussed above based on the overview TEM images (Figure 3c,d). The elongated segments remain stochiometric $CuInS_2$, while the $Cu_{2-x}S$ tips exhibit a Cu:S ratio of ~1.6 (Figure S9), which is comparable to that of the $Cu_{2-x}S$ tips of the HNCs after 10 min of reaction (*viz.*, 1.8 ± 0.1, Figure S7). It should be noted that the HNCs obtained after 30 min of reaction are apparently sulfur-rich (Figure S7), yielding unrealistically high S/In (*viz.* 3.1, Figure S7) and S/Cu ratios (*viz.* 3.3 and 1.0 in the copper indium sulfide and copper sulfide segments, respectively, Figure S7). The excess sulfur is also evident in the bulk EDX analysis of these samples (Figure S8) and can be attributed to residual 1-DDT and unreacted Cu and In thiolates, which are sometimes difficult to completely wash away due to their gel-forming propensity.[72] This is consistent with the higher background signal of S in the 30 min sample (Figure 4b). After a reaction time of 90 min, the HNCs are fully converted into homogeneous stoichiometric $CuInS_2$ nanorods (Figure S10).

The $Cu_{2-x}S/CuInS_2$ HNCs obtained after reaction times of 20 and 40 min were further analyzed by HRTEM (Figure 5a,b). In both cases, the FT patterns of the $CuInS_2$ segments can be indexed to the hexagonal wurtzite crystal structure, while those of the $Cu_{2-x}S$ tips are consistent with the monoclinic low-chalcocite Cu_2S. Similar analysis on other single $Cu_{2-x}S/CuInS_2$ HNCs is presented in Figure S11. In all cases, the $Cu_{2-x}S$ tips have the monoclinic low-chalcocite crystal structure. Figure 5c shows an atomic model of a single HNC reconstructed from Figure 5b. The sharp heterointerface connects the (−204) plane of low-chalcocite $Cu_{2-x}S$ and the (002) plane of wurtzite $CuInS_2$, which have a small bulk lattice mismatch of ~2.6%. The same analysis was performed on other HNCs. It was found that the $CuInS_2$ segment typically attaches to the $Cu_{2-x}S$ segment through its (002) plane and grows along the *c* axis. However, the plane of low-chalcocite $Cu_{2-x}S$ that connects to the $CuInS_2$ segment varies from particle to particle. For instance, the monoclinic low-chalcocite $Cu_{2-x}S$ can also be connected through its (−2 −4 0) plane with the (0 0 −2) plane of hexagonal wurtzite $CuInS_2$, as exemplified in Figure S11a. The XRD pattern of the product $Cu_{2-x}S/CuInS_2$ HNCs after 40 min of reaction is dominated by the diffraction peaks of the hexagonal wurtzite $CuInS_2$ without significant contributions from the $Cu_{2-x}S$ tips (Figure S12), which is due to the small volume of the $Cu_{2-x}S$ tips with respect to that of $CuInS_2$ (the volume of the $CuInS_2$ segments is over 7 times larger than that of $Cu_{2-x}S$ tips).

The TEM images discussed above (Figure 3b) show that the diameter of the $Cu_{2-x}S/CuInS_2$ HNCs is similar to the diameter of $Cu_{2-x}S$ seed NCs. This observation, combined with the EDS maps (Figure 4a,b), suggests that the $CuInS_2$ segments grow on either the top or bottom facets of the $Cu_{2-x}S$ nanoplatelets used as seeds. It is, however, possible that the $Cu_{2-x}S$ seed NCs undergo a structural reconstruction after the cation-exchange step and prior to the onset of the epitaxial growth of $CuInS_2$, similar to previous observations on the heteroepitaxial growth of wurtzite ZnS on high-chalcocite Cu_2S seed NCs.[30] Therefore, the unambiguous identification of the crystallographic nature of the facets where the $CuInS_2$ formation starts (*i.e.*, those where the initial Cu^+ for In^{3+} cation exchange occurs) would require advanced high-resolution TEM studies of the early stage samples (such as those shown in Figure 2). This is, however, precluded by the high electron beam sensitivity of these samples, which contain higher amounts of unreacted precursors that were not completely eliminated by the washing procedures (see discussion above). It should also be noted that the crystal structure of the $Cu_{2-x}S$ seed NCs during the reaction at 240 °C is most likely hexagonal high chalcocite, since this phase is more stable at high temperatures (see Figure 1 and discussion above). The growth of wurtzite $CuInS_2$ on the seed NCs would thus be favored since the hexagonal sulfide sublattices of high chalcocite and wurtzite are very similar.[52] Due to the reversibility of the low- to high-chalcocite phase transition,[75,76] the $Cu_{2-x}S$ tips of the HNCs adopt the low-chalcocite crystal structure when the reaction system is cooled to room temperature. This phase transition is fully compatible with the preservation of the high-chalcocite $Cu_{2-x}S$/wurtzite $CuInS_2$ heterointerface formed at 240 °C because the sulfide sublattices of high chalcocite and low chalcocite are very similar, since the two structures differ primarily regarding the distribution of the Cu^+ atoms through the available sites.[75] The adoption of the low-chalcocite crystal structure for copper-

https://doi.org/10.1021/acsnano.1c01488
ACS Nano 2021, 15, 9987−9999

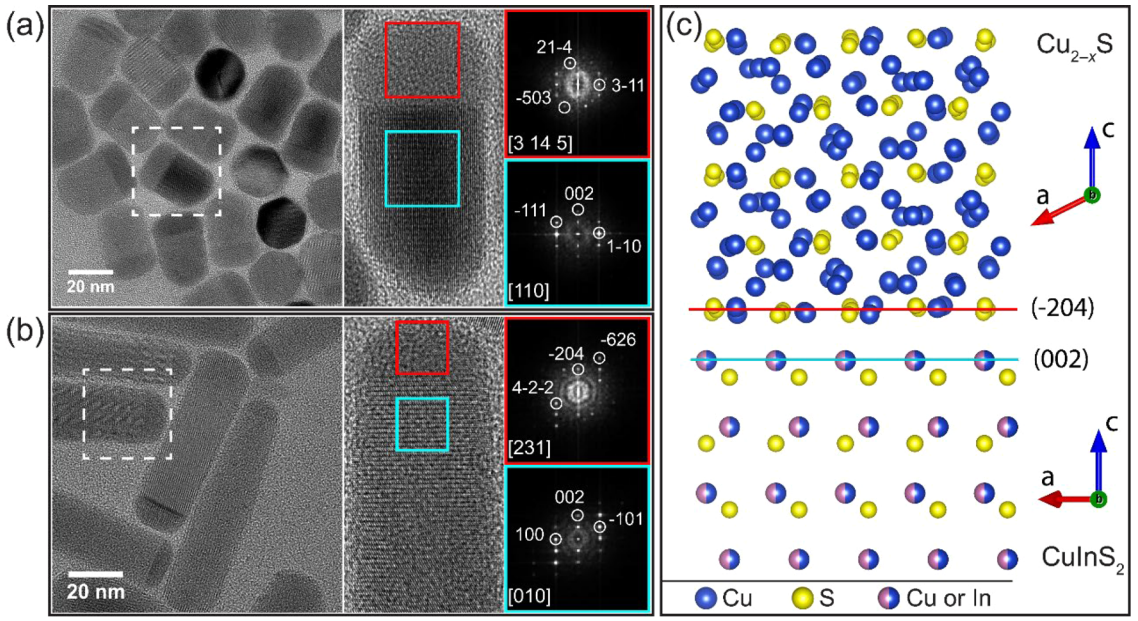

Figure 5. (a, b) HRTEM images of $Cu_{2-x}S/CuInS_2$ HNCs obtained by the injection of $Cu_{2-x}S$ seed NCs into a solution of indium oleate at 240 °C with reaction times of 20 min (a) and 40 min (b). Corresponding FT analyses of representative single $Cu_{2-x}S/CuInS_2$ HNCs (white dashed square) were performed on the right panel of a and b. The FT analyses were conducted on both the $Cu_{2-x}S$ parts (cyan square) and $CuInS_2$ parts (red square). The $Cu_{2-x}S$ tips can be indexed to the monoclinic low-chalcocite crystal structure and the $CuInS_2$ segments can be ascribed to the hexagonal wurtzite crystal structure. (c) Atomic structure of a $Cu_{2-x}S/CuInS_2$ HNC deduced from b. The monoclinic low-chalcocite $Cu_{2-x}S$ is connected through its (−204) plane with the (002) plane of hexagonal wurtzite $CuInS_2$.

deficient $Cu_{2-x}S$ stoichiometries (Cu/S ratio of the $Cu_{2-x}S$ tips varies from 1.8 ± 0.1 at 10 min to 1.6 ± 0.1 at 40 min, see above) is at first sight surprising, since bulk $Cu_{2-x}S$ in this compositional range adopts either the cubic digenite (x = 0.2) or the triclinic roxbyite (x = 0.14−0.25) crystal structures.[77] Nevertheless, this observation can be rationalized by considering the highly dynamic nature of Cu^+ in $Cu_{2-x}S$ phases[75] and the very rich phase diagram of the binary Cu−S system.[77] This makes nanoscale $Cu_{2-x}S$ very likely to adopt metastable crystal structures or to undergo phase transformations in response to external perturbations (e.g., surfactants,[68−70] oxidation,[66,68] size,[71,76] or heterointerfacial strain[29,39]).

In the multistage seeded-injection synthesis protocol developed in this work, the $Cu_{2-x}S$ seed NCs are the only source of copper and are therefore fully consumed if the reaction is allowed to reach completion (*i.e.*, formation of single composition wurtzite $CuInS_2$ nanorods, Figure 3). We have thus carried out control experiments to investigate the effect of injecting extra copper ions in solution together with the $Cu_{2-x}S$ seed NCs (see the Methods for details). The effect of the Cu oxidation state (*i.e.*, addition of Cu^+ or Cu^{2+}) and of different anions was also investigated (Figure S13). These experiments show that the addition of extra Cu(I) ions minimizes the consumption of the $Cu_{2-x}S$ seed NCs, resulting in $Cu_{2-x}S/CuInS_2$ HNCs with more pronounced $Cu_{2-x}S$ tips. For example, the average length (~15 nm) of $Cu_{2-x}S$ tips is twice that of $Cu_{2-x}S$ tips obtained without extra Cu(I) ions while their diameters are comparable (Figure S13a−c). However, addition of extra Cu^+ ions also leads to homogeneous nucleation of $Cu_{2-x}S$ NCs, which becomes more evident at higher concentrations (Figure S13c). This observation indicates that the formation of $CuInS_2$ by cation exchange and its subsequent epitaxial growth are relatively slow processes that are easily outcompeted by homogeneous nucleation of $Cu_{2-x}S$. The use of Cu^{2+} salts, which must be reduced to Cu^+ prior to $Cu_{2-x}S$ formation, does not significantly decrease the $Cu_{2-x}S$ nucleation rates but dramatically affects the $CuInS_2$ formation and growth rates leading to larger size and shape polydispersity (Figure S13d−f). In the presence of halides (*i.e.*, when CuI, CuBr, or CuCl are used as Cu^+ sources), $Cu_{2-x}S$ nanosheets are formed (Figure S13g−i) due to halide stabilization of Cu-thiolate 2D templates.[72,73]

Formation Mechanism of $Cu_{2-x}S/CuInS_2$ HNCs by Two-Stage Seeded Injection. The injection of $Cu_{2-x}S$ seed NCs and 1-DDT in a hot In oleate solution starts a series of coupled reactions that ultimately lead to the formation of Janus-type $Cu_{2-x}S/CuInS_2$ HNCs. The outcome of this chain of coupled reactions depends on a delicate kinetic balance between all the elementary steps involved, which is in turn determined by the changing reaction conditions, such as the concentrations of the different precursors. Based on the observations discussed above, we propose a mechanism for the formation of $Cu_{2-x}S/CuInS_2$ HNCs *via* seeded-injection, which is schematically represented in Figure 6 and discussed in detail below.

In the first step of the reaction, the as-prepared $Cu_{2-x}S$ seed NCs dispersed in 1-DDT are quickly injected in a solution of In oleate in oleic acid at 240 °C. As evidenced by the EDX maps (Figure 2a), 1 min after the injection of the $Cu_{2-x}S$/DDT mixture, no indium is incorporated in the $Cu_{2-x}S$ seed NCs. The formation of the HNCs is thus not directly initiated upon injecting the $Cu_{2-x}S$ seed NCs, suggesting that In oleate must first be converted to more reactive In^{3+}-species. It is well-known that In carboxylates (such as In acetate or In oleate) are converted to reactive In thiolate complexes if heated to sufficiently high temperatures (≥100 °C) in the presence of thiols.[78] We thus propose that the first step of the formation of $Cu_{2-x}S/CuInS_2$ HNCs by injection of $Cu_{2-x}S$ NC seeds is the

https://doi.org/10.1021/acsnano.1c01488
ACS Nano 2021, 15, 9987−9999

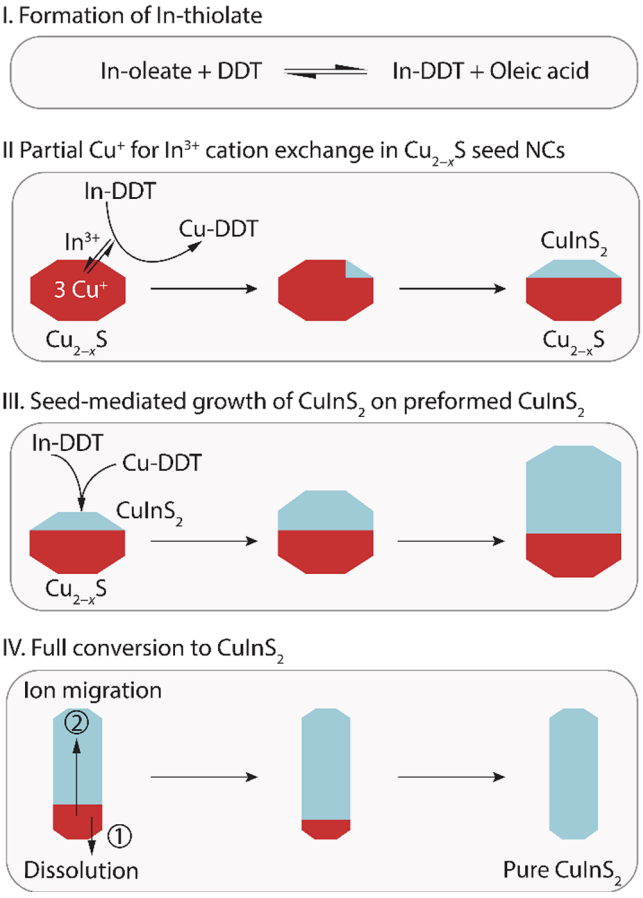

Figure 6. Schematic representation of the proposed formation mechanism for $Cu_{2-x}S/CuInS_2$ HNCs by injection of $Cu_{2-x}S$ seed NCs and 1-DDT in a hot solution of In oleate. In the first step, $Cu_{2-x}S$ seed NCs dispersed in DDT are injected, leading to the formation of In thiolate complexes. Subsequently, the formation of the HNCs is initiated by a single-step, thiolate-mediated Cu^+ for In^{3+} cation exchange (step II). The cation-exchange reaction is overtaken by the homoepitaxial growth of wurtzite $CuInS_2$ on the preformed $CuInS_2$ surface (step III). Eventually, the $Cu_{2-x}S$ tips disappear and pure $CuInS_2$ NCs are formed (step IV).

conversion of In oleate into In thiolate complexes by reaction with the injected DDT (step I, Figure 6).

Two minutes after the injection of the $Cu_{2-x}S$ seed NCs, a small corner of $CuInS_2$ is visible in most $Cu_{2-x}S$ seed NCs (Figure 2b), indicating the onset of the formation of HNCs (step II, Figure 6). The size and shape of the NCs is, however, not significantly changed (Figure 3b), indicating that the formation of the heterostructures is initiated by a topotactic cation-exchange reaction where Cu^+ is extracted from the NCs and In^{3+} is incorporated into the crystal, while the size and shape of the NC is preserved. Cation exchange requires a delicate balance of all reaction steps, *viz.,* cleavage of the bond between the incoming cation (In^{3+}) and the thiolate ligand, formation of an In−S bond, followed by In^{3+} diffusion into the NC, formation of a bond between the host-cation (Cu^+) and the thiolate ligand, cleavage of a Cu−S bond, and diffusion of the Cu thiolate complex from the NC into solution, leaving a Cu^+ vacancy that must be filled by Cu^+ diffusing to the surface to allow the reaction to proceed.[52] Ultimately, the driving force for the cation-exchange reaction is determined by the reactivities and stabilities of both the parent and product NCs, as well as of the cation complexes in solution.[50,52]

The delay prior to the start of the cation-exchange reaction can thus be explained by the requirement that first suitable precursors for the cation-exchange reaction must be formed. Prior to the injection, indium is present as In oleate, a stable complex of the hard Lewis acid In^{3+} (η = ∼13 eV)[79] with the hard Lewis base oleate. In addition, Cu^+ is a soft Lewis acid (η = 6.28 eV),[79] and hence, oleate is not a suitable extracting ligand for Cu^+, making the cation exchange unfavorable when only In oleate is present. As proposed above, when the suspension of $Cu_{2-x}S$ NCs in 1-DDT is injected into the hot In oleate solution, In thiolate complexes are formed by reaction between DDT and In oleate. According to the HSAB theory, In thiolate is a less stable complex than In oleate, while the formation of Cu(I) thiolate is favored since thiolate is a soft Lewis base (absolute hardness thiolate η = ∼ 6 eV).[61] This makes the thiolate-mediated single step Cu^+ for In^{3+} exchange favorable, provided a sufficiently high concentration of In thiolate is available. Once one Cu^+ ion is exchanged for an In^{3+} ion, the resulting charge imbalance in the NC will force two more Cu^+ ions out of the NC to balance the overall charge. This Cu^+ extraction leads to the formation of more Cu^+ vacancies in the NC, which in turn favors the diffusion of cations within the NC. The sufficiently high concentration of In thiolate complexes will then lead to the incorporation of more In^{3+}, which in turn will force more Cu^+ ions to diffuse out of the NC, and so a cascade of reactions is started. This can also explain the observation that the cation exchange always starts from one side of the NC: once the cation exchange is initiated at a certain point, it is most likely to proceed there because of the cascade of reactions.[50,80,81] It should be noted that topotactic partial Cu^+ for In^{3+} cation exchange in $Cu_{2-x}S$ NCs with crystal structures containing hcp sulfide sublattices (such as low and high chalcocite or roxbyite) has been shown to lead to the formation of wurtzite $CuInS_2$ NCs.[42−44,50−54]

At longer reaction times (>5 min), the shape and size of the NCs start to change (Figure 3), indicating that the reaction is no longer occurring *via* topotactic cation exchange (step III, Figure 6). Instead, the $Cu_{2-x}S/CuInS_2$ HNCs grow further *via* a seeded growth mechanism from Cu, In, and S monomers in solution. The cation exchange is thus terminated before the whole $Cu_{2-x}S$ seed NC is converted into $CuInS_2$. The heteroepitaxial growth of $CuInS_2$ directly on the $Cu_{2-x}S$ seed NCs is unfavorable due to the dynamic nature of the $Cu_{2-x}S$ NC surface, in which the Cu^+ ions are very mobile.[75] The in growth of a wurtzite $CuInS_2$ domain by topotactic partial Cu^+ for In^{3+} cation exchange in the first 5 min of reaction provides a stable $CuInS_2$ surface, onto which $CuInS_2$ can readily grow through homoepitaxy from Cu, In, and S precursors from solution. The observation that the cation exchange stops when the homoepitaxial growth of $CuInS_2$ starts implies that the latter has a lower energy barrier than the former under the conditions prevalent in our experiments (*i.e.*, absence of strong Cu^+-extracting agents). Therefore, homoepitaxial growth outcompetes Cu^+ for In^{3+} cation exchange for the limited supply of In−DDT complexes and the formation of the $Cu_{2-x}S/CuInS_2$ HNCs proceeds *via* seeded growth of wurtzite $CuInS_2$ from precursors in solution.

As discussed above, the $Cu_{2-x}S$ seed NCs are the only source of Cu^+ ions for the formation of $CuInS_2$. In the first phase of the reaction (cation exchange), Cu^+ is extracted from the NCs into solution, providing Cu^+ for the subsequent

https://doi.org/10.1021/acsnano.1c01488
ACS Nano 2021, 15, 9987−9999

growth of $CuInS_2$ in the second phase. However, the volume of the $CuInS_2$ segment after a reaction time of 30 min is much larger than the volume of the original $Cu_{2-x}S$ seed NCs, implying that, besides the Cu^+ originating from the cation-exchange reactions, additional Cu^+ must be present in solution. This additional Cu^+ likely originates from dissolution of part of the $Cu_{2-x}S$ seed NCs prior to the onset of the cation exchange and homoepitaxial growth phases. A control experiment, in which a suspension of $Cu_{2-x}S$ seed NCs in 1-DDT was injected into neat oleic acid at 240 °C (Figure S14), demonstrated that the $Cu_{2-x}S$ seed NCs are indeed susceptible to dissolution under these reaction conditions. However, we note that the dissolution in the presence of In oleate should be much less pronounced after the first minute of reaction due to the onset of the cation-exchange reactions and subsequent growth of $CuInS_2$.

At even longer reaction times (>30 min), the $Cu_{2-x}S$ tips start to shrink and eventually disappear (≤60 min), leaving single-component wurtzite $CuInS_2$ nanorods as the final reaction product (step IV, Figures 6, S6, and S10). Further changes to the $CuInS_2$ nanorods will then only occur by slow growth until the Cu and In thiolates remaining in solution are fully depleted. This slow growth phase is accompanied by pronounced internal ripening, resulting in icicle-shaped nanorods (Figure S6). The reduction of the volume of the $Cu_{2-x}S$ tips indicates that Cu^+ ions for the growth of $CuInS_2$ originate not only from the dissolution of $Cu_{2-x}S$ seed NCs prior to the onset of the formation of $CuInS_2$ but also from consumption of $Cu_{2-x}S$ tips during the epitaxial growth. The disappearance of $Cu_{2-x}S$ tips and the formation of single-component $CuInS_2$ nanorods can be rationalized by two possible pathways: (1) the depletion of Cu^+ ions by the growth of $CuInS_2$ leads to a low concentration of Cu^+ in solution, thereby eventually driving complete dissolution of the $Cu_{2-x}S$ tips, which are then used to further grow the $CuInS_2$; (2) the Cu^+ ions in the $Cu_{2-x}S$ lattice are highly mobile at high temperatures[75−77] and therefore diffuse to the heterointerface to form $CuInS_2$. These pathways imply that the fate of the $Cu_{2-x}S$ segment strongly depends on the available Cu^+ ions in the solution (see control experiments above, Figure S13) or in the $Cu_{2-x}S$ seed NCs. Lastly, prolonged reaction times do not induce the conversion of $CuInS_2$ NCs into In_2S_3 (Figure 6), because the Cu^+ for In^{3+} cation exchange in $Cu_{2-x}S$ NCs is self-limited, as demonstrated in previous reports.[52,54,61]

The mechanism proposed in the present work for the formation of $Cu_{2-x}S/CuInS_2$ HNCs by seeded growth differs from mechanisms previously proposed based on one-pot synthesis protocols in two important ways: (i) the first step consist of a topotactic partial Cu^+ for In^{3+} cation-exchange reaction, rather than a "catalyst-assisted" reaction as proposed in refs 37, 40, and 41. The "catalyst-assisted" mechanism assumes that In^{3+} dissolves into the (*in situ* formed) $Cu_{2-x}S$ seed NCs until the solubility limit of the $CuInS_2$ phase is exceeded, causing its phase separation. This assumption is inconsistent with the observations discussed above (the $CuInS_2$ domain is directly formed, and the remaining $Cu_{2-x}S$ domains are In free). (ii) The $CuInS_2$ growth proceeds by homoepitaxy, rather than heteroepitaxy as proposed in *e.g.*, ref 36.

CONCLUSIONS

In this work, a two-step synthesis route to Janus-type $Cu_{2-x}S/CuInS_2$ HNCs is developed. The $Cu_{2-x}S/CuInS_2$ HNCs were obtained by injecting preformed $Cu_{2-x}S$ seed NCs, dispersed in 1-DDT, into a hot indium oleate solution. By making use of preformed $Cu_{2-x}S$ seed NCs, the two stages of the $Cu_{2-x}S/CuInS_2$ HNC formation were separated. This allowed for the synthesis of anisotropic HNCs with tunable size, shape, and composition, and small polydispersity. Interestingly, elemental mapping of the product NCs obtained in the first few minutes of reaction suggests that the formation of the $Cu_{2-x}S/CuInS_2$ HNCs is initiated by a single-step, thiolate-mediated topotactic Cu^+ for In^{3+} exchange which results in the formation of a wurtzite $CuInS_2$ domain on one side of the $Cu_{2-x}S$ seed NCs. At longer reaction times, the cation-exchange reaction is overtaken by homoepitaxial growth of wurtzite $CuInS_2$ on the preformed $CuInS_2$ surface. The good control over size, shape, and composition of the HNCs offered by this method allowed for the formation of well-defined Janus-type $Cu_{2-x}S/CuInS_2$ HNCs that are of potential interest for applications such as photovoltaics and photocatalysis. The two-stage seeded-injection synthesis strategy developed here contributes toward the rational synthesis of $Cu_{2-x}S/CuInS_2$ HNCs by allowing one to leverage on the knowledge available on both seeded-injection[1,4,30,47,48,55−58,61] and cation-exchange[16,30,47−53] synthesis protocols and the high degree of control already achieved over the size, shape, and crystal structure of $Cu_{2-x}S$ NCs[16,30,54,62−73] to tailor the $Cu_{2-x}S/CuInS_2$ HNCs. Follow-up work should thus be directed toward exploring the impact of using $Cu_{2-x}S$ seed NCs with different sizes, shapes and crystal structures and on modulating the balance between cation exchange and epitaxial growth.

METHODS

Materials. Indium nitrate hydrate ($In(NO_3)_3{\cdot}xH_2O$, 99.9%), copper(I) acetate (CuOAc, 97%), copper acetylacetonate ($Cu(acac)_2$, 97%), copper(I) iodide (CuI, 98%), copper(I) bromide (CuBr, 98%), copper(I) chloride (CuCl, 99%), 1-dodecanethiol (1-DDT, ≥98%), oleic acid (OA, 90%), oleylamine (OLAM, 70%), anhydrous toluene, methanol, butanol, and ethanol were purchased from Sigma-Aldrich and used as received.

One-Pot Direct Synthesis of $Cu_{2-x}S/CuInS_2$ HNCs. As a control experiment, $Cu_{2-x}S/CuInS_2$ HNCs were also prepared without using preformed $Cu_{2-x}S$ seed NCs. Briefly, $In(NO_3)_3{\cdot}xH_2O$ (0.06 g, 0.2 mmol) was mixed with 4 mL of OA in a three-neck flask. The $In(NO_3)_3$−OA mixture was degassed for 30 min at 120 °C and then heated to 240 °C at a rate of ∼20 °C/min under nitrogen protection. At 240 °C, a solution of CuOAc (0.025 g, 0.2 mmol) in 5 mL of 1-DDT was rapidly injected into the hot solution and the mixture was allowed to react for various times. To stop the reaction, the heating was turned off and the mixture was naturally cooled down and washed with an excess of ethanol followed by centrifugation at 2750 rpm for 10 min. The $Cu_{2-x}S/CuInS_2$ HNCs were redispersed in toluene and stored in a glovebox.

Two-Stage Seeded-Injection Synthesis of $Cu_{2-x}S/CuInS_2$ HNCs. Prior to the seeded-injection synthesis, $Cu_{2-x}S$ seed NCs were prepared according to a previously reported method.[67] $Cu(acac)_2$ (0.79 g, 3 mmol), 15 mL of OLAM, and 15 mL of 1-DDT were mixed and gradually heated to 200 °C under N_2 protection using a standard Schlenk line. The mixture was kept at this temperature for 2 h before naturally cooling to room temperature. The products were washed three times by addition of an excess of isometric methanol and butanol solution, followed by centrifugation at 2750 rpm for 10 min. The yielded $Cu_{2-x}S$ NC precipitates were redispersed in 12 mL of anhydrous toluene and stored in a glovebox for further use.

For a typical seeded-injection reaction, 1 mL of the $Cu_{2-x}S$ seed NC stock solution was precipitated using an excess of isometric methanol and butanol solution, followed by centrifugation at 2750

https://doi.org/10.1021/acsnano.1c01488
ACS Nano 2021, 15, 9987−9999

rpm for 10 min. The NCs were redispersed in 5 mL of 1-DDT. Meanwhile, $In(NO_3)_3 \cdot x\ H_2O$ (0.06 g, 0.2 mmol) was mixed with 4 mL of OA and degassed for 30 min at 120 °C. The $In(NO_3)_3$−OA mixture was then heated to 240 °C under nitrogen protection. At 240 °C, the as-prepared $Cu_{2-x}S$ seed NC solution was rapidly injected into the hot solution and the mixture was allowed to react for various times (1−90 min). The reaction mixture was then naturally cooled down and washed with an excess of ethanol using the same washing procedures described above. The product $Cu_{2-x}S/CuInS_2$ HNCs were finally redispersed in 5 mL of toluene and stored in a glovebox.

Control Experiments. To investigate the influence of extra Cu(I) precursors on the reaction, different amounts of CuOAc or Cu halides were first dissolved into 5 mL of 1-DDT. The effect of the Cu oxidation state and of the anion was studied by dissolving either $Cu(OAc)_2$ or $Cu(acac)_2$ in 1-DDT. To keep the control experiments consistent with both the multistage seeded-injection and the one-pot protocols the resulting solutions were then mixed with the $Cu_{2-x}S$ seed NCs and injected into the $In(NO_3)_3$−OA mixture at 240 °C, while keeping all other parameters unchanged. The simultaneous injection of the excess copper salts and the $Cu_{2-x}S$ seed NCs into the hot indium oleate solution is also expected to minimize homogeneous nucleation of $Cu_{2-x}S$ NCs while kinetically favoring the onset of the cation exchange reaction on the preformed seeds.

Characterization. Samples for transmission electron microscopy (TEM) analysis were prepared by drop-casting a solution of $Cu_{2-x}S/CuInS_2$ HNCs in toluene on carbon-coated 200 mesh copper or aluminum TEM grids. TEM analysis was performed using a FEI-Technai 12 microscope operating at 100 kV or a FEI Technai 20 microscope operating at 200 kV. High-resolution TEM (HRTEM) images and elemental maps were recorded for samples on aluminum grids using a FEI Talos F200x transmission electron microscope (Thermo Fisher Scientific), operated at 200 kV. The elemental maps were collected in an area of 1024 × 1024 pixels with an acquisition time of 5−10 min using Esprit software from Bruker. The elemental quantification is done by adding up all the counts in the entire spectrum for each channel and all pixels within the area of interest. Samples for X-ray diffraction (XRD) analysis were prepared by uniformly spreading dried NCs powder (~0.1 g) over a silicon wafer. XRD measurements at room temperature were performed with a Bruker D2 Phaser, equipped with a Co K X-ray source with a wavelength of 1.79026 Å. The temperature-dependent XRD measurements were performed using a Bruker D8, equipped with a Co K X-ray source with a wavelength of 1.79026 Å. These measurements were performed under an argon flow at temperatures of 28, 49, 74, 90, 100, 110, 149, 199, 224, 240, 250 °C with a heating ramp of 5 °C/min.

ASSOCIATED CONTENT

Supporting Information

The Supporting Information is available free of charge at https://pubs.acs.org/doi/10.1021/acsnano.1c01488.

TEM images and elemental maps of $Cu_{2-x}S/CuInS_2$ HNCs synthesized with and without $Cu_{2-x}S$ seed NCs; XRD patterns of the $Cu_{2-x}S$ seed NCs recorded at different temperatures; XRD pattern of the $Cu_{2-x}S/CuInS_2$ HNCs prepared with a reaction time of 40 min; HRTEM images and corresponding FT analyses of $Cu_{2-x}S/CuInS_2$ HNCs; TEM images of $Cu_{2-x}S/CuInS_2$ HNCs synthesized by addition of extra copper precursors to the seeded injection at 240 °C (PDF)

AUTHOR INFORMATION

Corresponding Author

Celso de Mello Donega − *Condensed Matter and Interfaces, Debye Institute for Nanomaterials Science, Utrecht University, 3508 TA Utrecht, The Netherlands;* orcid.org/0000-0002-4403-3627; Email: c.demello-donega@uu.nl

Authors

Chenghui Xia − *Condensed Matter and Interfaces, Debye Institute for Nanomaterials Science, Utrecht University, 3508 TA Utrecht, The Netherlands;* Present Address: Laboratoire Photonique Numérique et Nanosciences (LP2N), Institut d'Optique & CNRS & Univ Bordeaux, UMR 5298, F-33400 Talence, France.; orcid.org/0000-0001-5087-8805

Christina H. M. van Oversteeg − *Condensed Matter and Interfaces, Debye Institute for Nanomaterials Science, Utrecht University, 3508 TA Utrecht, The Netherlands; Materials Chemistry and Catalysis, Debye Institute for Nanomaterials Science, Utrecht University, 3508 TA Utrecht, The Netherlands*

Veerle C. L. Bogaards − *Condensed Matter and Interfaces, Debye Institute for Nanomaterials Science, Utrecht University, 3508 TA Utrecht, The Netherlands*

Tim H. M. Spanjersberg − *Condensed Matter and Interfaces, Debye Institute for Nanomaterials Science, Utrecht University, 3508 TA Utrecht, The Netherlands*

Nienke L. Visser − *Condensed Matter and Interfaces, Debye Institute for Nanomaterials Science, Utrecht University, 3508 TA Utrecht, The Netherlands; Materials Chemistry and Catalysis, Debye Institute for Nanomaterials Science, Utrecht University, 3508 TA Utrecht, The Netherlands*

Anne C. Berends − *Condensed Matter and Interfaces, Debye Institute for Nanomaterials Science, Utrecht University, 3508 TA Utrecht, The Netherlands;* Present Address: Seaborough Research B.V., Science Park 106, 1098XG Amsterdam, The Netherlands.; orcid.org/0000-0003-4249-2843

Johannes D. Meeldijk − *Materials Chemistry and Catalysis, Debye Institute for Nanomaterials Science, Utrecht University, 3508 TA Utrecht, The Netherlands*

Petra E. de Jongh − *Materials Chemistry and Catalysis, Debye Institute for Nanomaterials Science, Utrecht University, 3508 TA Utrecht, The Netherlands;* orcid.org/0000-0002-2216-2620

Complete contact information is available at: https://pubs.acs.org/10.1021/acsnano.1c01488

Author Contributions

[⊥]C.X. and C.H.M.v.O. contributed equally.

Notes

The authors declare no competing financial interest.

ACKNOWLEDGMENTS

This work was supported by The Netherlands Center for Multiscale Catalytic Energy Conversion (MCEC), an NWO Gravitation program funded by the Ministry of Education, Culture and Science of the government of The Netherlands. C.X. thanks the China Scholarship Council (CSC) for financial support (grant number 201406330055). C.d.M.D. acknowledges financial support from the division of Chemical Sciences (CW) of The Netherlands Organization for Scientific Research (NWO) under Grant Nos. ECHO.712.012.0001 and ECHO.712.014.001. Dennie Wezendonk is acknowledged for his help with the high-temperature XRD measurements.

REFERENCES

(1) Cozzoli, P. D.; Pellegrino, T.; Manna, L. Synthesis, Properties and Perspectives of Hybrid Nanocrystal Structures. *Chem. Soc. Rev.* **2006**, *35*, 1195−1208.

(2) Reiss, P.; Protière, M.; Li, L. Core/Shell Semiconductor Nanocrystals. *Small* **2009**, *5*, 154−168.

(3) Costi, R.; Saunders, A. E.; Banin, U. Colloidal Hybrid Nanostructures: A New Type of Functional Materials. *Angew. Chem., Int. Ed.* **2010**, *49*, 4878−4897.

(4) de Mello Donegá, C. Synthesis and Properties of Colloidal Heteronanocrystals. *Chem. Soc. Rev.* **2011**, *40*, 1512−1546.

(5) Zhu, H.; Lian, T. Wavefunction Engineering in Quantum Confined Semiconductor Nanoheterostructures for Efficient Charge Separation and Solar Energy Conversion. *Energy Environ. Sci.* **2012**, *5*, 9406−9418.

(6) Wu, K.; Lian, T. Quantum Confined Colloidal Nanorod Heterostructures for Solar-to-Fuel Conversion. *Chem. Soc. Rev.* **2016**, *45*, 3781−3810.

(7) Kodaimati, M. S.; McClelland, K. P.; He, C.; Lian, S.; Jiang, Y.; Zhang, Z.; Weiss, E. A. Viewpoint: Challenges in Colloidal Photocatalysis and Some Strategies for Addressing Them. *Inorg. Chem.* **2018**, *57*, 3659−3670.

(8) Moroz, P.; Boddy, A.; Zamkov, M. Challenges and Prospects of Photocatalytic Applications Utilizing Semiconductor Nanocrystals. *Front. Chem.* **2018**, *6*, 353.

(9) Rainò, G.; Stöferle, T.; Moreels, I.; Gomes, R.; Kamal, J. S.; Hens, Z.; Mahrt, R. F. Probing the Wave Function Delocalization in CdSe/CdS Dot-in-Rod Nanocrystals by Time-and Temperature-Resolved Spectroscopy. *ACS Nano* **2011**, *5*, 4031−4036.

(10) Wu, K.; Rodríguez-Córdoba, W. E.; Liu, Z.; Zhu, H.; Lian, T. Beyond Band Alignment: Hole Localization Driven Formation of Three Spatially Separated Long-Lived Exciton States in CdSe/CdS Nanorods. *ACS Nano* **2013**, *7*, 7173−7185.

(11) Bridewell, V. L.; Alam, R.; Karwacki, C. J.; Kamat, P. V. CdSe/CdS Nanorod Photocatalysts: Tuning the Interfacial Charge Transfer Process through Shell Length. *Chem. Mater.* **2015**, *27*, 5064−5071.

(12) Dorfs, D.; Salant, A.; Popov, I.; Banin, U. ZnSe Quantum Dots within CdS Nanorods: A Seeded-Growth Type-II System. *Small* **2008**, *4*, 1319−1323.

(13) Kirsanova, M.; Nemchinov, A.; Hewa-Kasakarage, N. N.; Schmall, N.; Zamkov, M. Synthesis of ZnSe/CdS/ZnSe Nanobarbells Showing Photoinduced Charge Separation. *Chem. Mater.* **2009**, *21*, 4305−4309.

(14) Oh, N.; Kim, B. H.; Cho, S.-Y.; Nam, S.; Rogers, S. P.; Jiang, Y.; Flanagan, J. C.; Zhai, Y.; Kim, J.-H.; Lee, J.; Yu, Y.; Cho, Y. K.; Hur, G.; Zhang, J.; Trefonas, P.; Rogers, J. A.; Shim, M. Double-Heterojunction Nanorod Light-Responsive LEDs for Display Applications. *Science* **2017**, *355*, 616−619.

(15) Nanayakkara, S. U.; Cohen, G.; Jiang, C.-S.; Romero, M. J.; Maturova, K.; Al-Jassim, M.; van de Lagemaat, J.; Rosenwaks, Y.; Luther, J. M. Built-In Potential and Charge Distribution within Single Heterostructured Nanorods Measured by Scanning Kelvin Probe Microscopy. *Nano Lett.* **2013**, *13*, 1278−1284.

(16) van der Stam, W.; Berends, A. C.; de Mello Donegá, C. Prospects of Colloidal Copper Chalcogenide Nanocrystals. *ChemPhysChem* **2016**, *17*, 559−581.

(17) Jia, G.; Pang, Y.; Ning, J.; Banin, U.; Ji, B. Heavy-Metal-Free Colloidal Semiconductor Nanorods: Recent Advances and Future Perspectives. *Adv. Mater.* **2019**, *31*, 1900781.

(18) Hashimoto, Y.; Takeuchi, K.; Ito, K. Band Alignment at CdS/$CuInS_2$ Heterojunction. *Appl. Phys. Lett.* **1995**, *67*, 980−982.

(19) Liu, G.; Schulmeyer, T.; Thissen, A.; Klein, A.; Jaegermann, W. *In Situ* Preparation and Interface Characterization of TiO_2/Cu_2S Heterointerface. *Appl. Phys. Lett.* **2003**, *82*, 2269−2271.

(20) Liu, G.; Schulmeyer, T.; Brötz, J.; Klein, A.; Jaegermann, W. Interface Properties and Band Alignment of Cu_2S/CdS Thin Film Solar Cells. *Thin Solid Films* **2003**, *431*−*432*, 477−482.

(21) Binsma, J. J. M.; Giling, L. J.; Bloem, J. Luminescence of $CuInS_2$: I. The Broad Band Emission and Its Dependence on The Defect Chemistry. *J. Lumin.* **1982**, *27*, 35−53.

(22) Ueng, H. Y.; Hwang, H. L. The Defect Structure of $CuInS_2$. Part I: Intrinsic Defects. *J. Phys. Chem. Solids* **1989**, *50*, 1297−1305.

(23) Chen, H.; Wang, C. Y.; Wang, J. T.; Hu, X. P.; Zhou, S. X. First-Principles Study of Point Defects in Solar Cell Semiconductor $CuInS_2$. *J. Appl. Phys.* **2012**, *112*, 084513.

(24) Berends, A. C.; Mangnus, M. J. J.; Xia, C.; Rabouw, F. T.; de Mello Donega, C. Optoelectronic Properties of Ternary I−III−VI_2 Semiconductor Nanocrystals: Bright Prospects with Elusive Origins. *J. Phys. Chem. Lett.* **2019**, *10*, 1600−1616.

(25) Yi, L.; Tang, A.; Niu, M.; Han, W.; Hou, Y.; Gao, M. Synthesis and Self-Assembly of $Cu_{1.94}S$-ZnS Heterostructured Nanorods. *CrystEngComm* **2010**, *12*, 4124−4130.

(26) Han, S.-K.; Gong, M.; Yao, H.-B.; Wang, Z.-M.; Yu, S.-H. One-Pot Controlled Synthesis of Hexagonal-Prismatic $Cu_{1.94}S$-ZnS, $Cu_{1.94}S$-ZnS-$Cu_{1.94}S$, and $Cu_{1.94}S$-ZnS-$Cu_{1.94}S$-ZnS-$Cu_{1.94}S$ Heteronanostructures. *Angew. Chem., Int. Ed.* **2012**, *51*, 6365−6368.

(27) Huang, F.; Wang, X.; Xu, J.; Chen, D.; Wang, Y. A Plasmonic Nano-Antenna with Controllable Resonance Frequency: $Cu_{1.94}S$-ZnS Dimeric Nanoheterostructure Synthesized in Solution. *J. Mater. Chem.* **2012**, *22*, 22614−22618.

(28) Ye, H.; Tang, A.; Huang, L.; Wang, Y.; Yang, C.; Hou, Y.; Peng, H.; Zhang, F.; Teng, F. Facile One-Step Synthesis and Transformation of Cu(I)-Doped Zinc Sulfide Nanocrystals to $Cu_{1.94}S$−ZnS Heterostructured Nanocrystals. *Langmuir* **2013**, *29*, 8728−8735.

(29) Ha, D.-H.; Caldwell, A. H.; Ward, M. J.; Honrao, S.; Mathew, K.; Hovden, R.; Koker, M. K. A.; Muller, D. A.; Hennig, R. G.; Robinson, R. D. Solid−Solid Phase Transformations Induced through Cation Exchange and Strain in 2D Heterostructured Copper Sulfide Nanocrystals. *Nano Lett.* **2014**, *14*, 7090−7099.

(30) Xia, C.; Pedrazo-Tardajos, A.; Wang, D.; Meeldijk, J. D.; Gerritsen, H. C.; Bals, S.; de Mello Donega, C. Seeded Growth Combined with Cation Exchange for the Synthesis of Anisotropic $Cu_{2-x}S$/ZnS, $Cu_{2-x}S$, and $CuInS_2$ Nanorods. *Chem. Mater.* **2021**, *33*, 102−116.

(31) Zhou, J.; Huang, F.; Xu, J.; Wang, Y. $Cu_{1.94}S$-MnS Dimeric Nanoheterostructures with Bifunctions: Localized Surface Plasmon Resonance and Magnetism. *CrystEngComm* **2013**, *15*, 4217−4220.

(32) Regulacio, M. D.; Ye, C.; Lim, S. H.; Bosman, M.; Polavarapu, L.; Koh, W. L.; Zhang, J.; Xu, Q.-H.; Han, M.-Y. One-Pot Synthesis of $Cu_{1.94}S$−CdS and $Cu_{1.94}S$−$Zn_xCd_{1-x}S$ Nanodisk Heterostructures. *J. Am. Chem. Soc.* **2011**, *133*, 2052−2055.

(33) Zhuang, T.-T.; Fan, F.-J.; Gong, M.; Yu, S.-H. $Cu_{1.94}S$ Nanocrystal Seed Mediated Solution-Phase Growth of Unique Cu_2S−PbS Heteronanostructures. *Chem. Commun.* **2012**, *48*, 9762−9764.

(34) Choi, S.-H.; Kim, E.-G.; Hyeon, T. One-Pot Synthesis of Copper−Indium Sulfide Nanocrystal Heterostructures with Acorn, Bottle, and Larva Shapes. *J. Am. Chem. Soc.* **2006**, *128*, 2520−2521.

(35) Han, W.; Yi, L.; Zhao, N.; Tang, A.; Gao, M.; Tang, Z. Synthesis and Shape-Tailoring of Copper Sulfide/Indium Sulfide-Based Nanocrystals. *J. Am. Chem. Soc.* **2008**, *130*, 13152−13161.

(36) Connor, S. T.; Hsu, C.-M.; Weil, B. D.; Aloni, S.; Cui, Y. Phase Transformation of Biphasic Cu_2S−$CuInS_2$ to Monophasic $CuInS_2$ Nanorods. *J. Am. Chem. Soc.* **2009**, *131*, 4962−4966.

(37) Kruszynska, M.; Borchert, H.; Parisi, J.; Kolny-Olesiak, J. Synthesis and Shape Control of $CuInS_2$ Nanoparticles. *J. Am. Chem. Soc.* **2010**, *132*, 15976−15986.

(38) Lu, X.; Zhuang, Z.; Peng, Q.; Li, Y. Controlled Synthesis of Wurtzite $CuInS_2$ Nanocrystals and Their Side-by-Side Nanorod Assemblies. *CrystEngComm* **2011**, *13*, 4039−4045.

(39) Chang, J.-Y.; Cheng, C.-Y. Facile One-Pot Synthesis of Copper Sulfide−Metal Chalcogenide Anisotropic Heteronanostructures in a Noncoordinating Solvent. *Chem. Commun.* **2011**, *47*, 9089−9091.

(40) Li, J.; Bloemen, M.; Parisi, J.; Kolny-Olesiak, J. Role of Copper Sulfide Seeds in the Growth Process of $CuInS_2$ Nanorods and Networks. *ACS Appl. Mater. Interfaces* **2014**, *6*, 20535−20543.

https://doi.org/10.1021/acsnano.1c01488
ACS Nano 2021, 15, 9987−9999

(41) Kolny-Olesiak, J. Synthesis of Copper Sulphide-Based Hybrid Nanostructures and Their Application in Shape Control of Colloidal Semiconductor Nanocrystals. *CrystEngComm* **2014**, *16*, 9381−9390.
(42) Mu, L.; Wang, F.; Sadtler, B.; Loomis, R. A.; Buhro, W. E. Influence of the Nanoscale Kirkendall Effect on the Morphology of Copper Indium Disulfide Nanoplatelets Synthesized by Ion Exchange. *ACS Nano* **2015**, *9*, 7419−7428.
(43) Lee, S.; Baek, S.; Park, J. P.; Park, J. H.; Hwang, D. Y.; Kwak, S. K.; Kim, S.-W. Transformation from $Cu_{2-x}S$ Nanodisks to $Cu_{2-x}S$@ $CuInS_2$ Heteronanodisks *via* Cation Exchange. *Chem. Mater.* **2016**, *28*, 3337−3344.
(44) Zhai, Y.; Flanagan, J. C.; Shim, M. Lattice Strain and Ligand Effects on the Formation of $Cu_{2-x}S$/I-III-VI_2 Nanorod Heterostructures through Partial Cation Exchange. *Chem. Mater.* **2017**, *29*, 6161−6167.
(45) Li, Y.; Tang, A.; Liu, Z.; Peng, L.; Yuan, Y.; Shi, X.; Yang, C.; Teng, F. Formation of Uniform Carrot-Like $Cu_{31}S_{16}$−$CuInS_2$ Heteronanostructures Assisted by Citric Acid at the Oil/Aqueous Interface. *Dalton Trans* **2018**, *47*, 67−73.
(46) Li, Y.; Liu, J.; Li, X.; Wan, X.; Pan, R.; Rong, H.; Liu, J.; Chen, W.; Zhang, J. Evolution of Hollow $CuInS_2$ Nanododecahedrons *via* Kirkendall Effect Driven by Cation Exchange for Efficient Solar Water Splitting. *ACS Appl. Mater. Interfaces* **2019**, *11*, 27170−27177.
(47) Berends, A. C.; van der Stam, W.; Hofmann, J. P.; Bladt, E.; Meeldijk, J. D.; Bals, S.; de Mello Donega, C. Interplay between Surface Chemistry, Precursor Reactivity, and Temperature Determines Outcome of ZnS Shelling Reactions on $CuInS_2$ Nanocrystals. *Chem. Mater.* **2018**, *30*, 2400−2413.
(48) Xia, C.; Winckelmans, N.; Prins, P. T.; Bals, S.; Gerritsen, H. C.; de Mello Donegá, C. Near-Infrared-Emitting $CuInS_2$/ZnS Dot-in-Rod Colloidal Heteronanorods by Seeded Growth. *J. Am. Chem. Soc.* **2018**, *140*, 5755−5763.
(49) van der Stam, W.; Bladt, E.; Rabouw, F. T.; Bals, S.; de Mello Donega, C. Near-Infrared Emitting $CuInSe_2$/$CuInS_2$ Dot Core/Rod Shell Heteronanorods by Sequential Cation Exchange. *ACS Nano* **2015**, *9*, 11430−11438.
(50) De Trizio, L.; Manna, L. Forging Colloidal Nanostructures *via* Cation Exchange Reactions. *Chem. Rev.* **2016**, *116*, 10852−10887.
(51) Liu, Y.; Liu, M.; Yin, D.; Qiao, L.; Fu, Z.; Swihart, M. T. Selective Cation Incorporation into Copper Sulfide Based Nanoheterostructures. *ACS Nano* **2018**, *12*, 7803−7811.
(52) van der Stam, W.; Berends, A. C.; Rabouw, F. T.; Willhammar, T.; Ke, X.; Meeldijk, J. D.; Bals, S.; de Mello Donegá, C. Luminescent $CuInS_2$ Quantum Dots by Partial Cation Exchange in $Cu_{2-x}S$ Nanocrystals. *Chem. Mater.* **2015**, *27*, 621−628.
(53) Steimle, B. C.; Fenton, J. L.; Schaak, R. E. Rational Construction of A Scalable Heterostructured Nanorod Megalibrary. *Science* **2020**, *367*, 418−424.
(54) Xia, C.; Wu, W.; Yu, T.; Xie, X.; van Oversteeg, C.; Gerritsen, H. C.; de Mello Donega, C. Size-Dependent Band-Gap and Molar Absorption Coefficients of Colloidal $CuInS_2$ Quantum Dots. *ACS Nano* **2018**, *12*, 8350−8361.
(55) Talapin, D. V.; Nelson, J. H.; Shevchenko, E. V.; Aloni, S.; Sadtler, B.; Alivisatos, A. P. Seeded Growth of Highly Luminescent CdSe/CdS Nanoheterostructures with Rod and Tetrapod Morphologies. *Nano Lett.* **2007**, *7*, 2951−2959.
(56) Carbone, L.; Nobile, C.; De Giorgi, M.; Sala, F. D.; Morello, G.; Pompa, P.; Hytch, M.; Snoeck, E.; Fiore, A.; Franchini, I. R. Synthesis and Micrometer-Scale Assembly of Colloidal CdSe/CdS Nanorods Prepared by a Seeded Growth Approach. *Nano Lett.* **2007**, *7*, 2942−2950.
(57) Nakonechnyi, I.; Sluydts, M.; Justo, Y.; Jasieniak, J.; Hens, Z. Mechanistic Insights in Seeded Growth Synthesis of Colloidal Core/Shell Quantum Dots. *Chem. Mater.* **2017**, *29*, 4719−4727.
(58) Zhu, D.; Ye, H.; Liu, Z.; Liu, J.; Fu, H.; Huang, Y.; Teng, F.; Wang, Z.; Tang, A. Seed-Mediated Growth of Heterostructured $Cu_{1.94}S$−MS (M = Zn, Cd, Mn) and Alloyed $CuNS_2$ (N = In, Ga) Nanocrystals for Use in Structure- and Composition-Dependent Photocatalytic Hydrogen Evolution. *Nanoscale* **2020**, *12*, 6111−6120.
(59) Sakamoto, M.; Inoue, K.; Okano, M.; Saruyama, M.; Kim, S.; So, Y.-G.; Kimoto, K.; Kanemitsu, Y.; Teranishi, T. Light-Stimulated Carrier Dynamics of $CuInS_2$/CdS Heterotetrapod Nanocrystals. *Nanoscale* **2016**, *8*, 9517−9520.
(60) Kim, B.; Kim, K.; Kwon, Y.; Lee, W.; Shin, W. H.; Kim, S.; Bang, J. $CuInS_2$/CdS-Heterostructured Nanotetrapods by Seeded Growth and Their Photovoltaic Properties. *ACS Appl. Nano Mater.* **2018**, *1*, 2449−2454.
(61) Xia, C.; Meeldijk, J. D.; Gerritsen, H. C.; de Mello Donegá, C. Highly Luminescent Water-Dispersible NIR-Emitting Wurtzite $CuInS_2$/ZnS Core/Shell Colloidal Quantum Dots. *Chem. Mater.* **2017**, *29*, 4940−4951.
(62) Kruszynska, M.; Borchert, H.; Bachmatiuk, A.; Rümmeli, M. H.; Büchner, B.; Parisi, J.; Kolny-Olesiak, J. Size and Shape Control of Colloidal Copper(I) Sulfide Nanorods. *ACS Nano* **2012**, *6*, 5889−5896.
(63) Robinson, E. H.; Turo, M. J.; Macdonald, J. E. Controlled Surface Chemistry for the Directed Attachment of Copper(I) Sulfide Nanocrystals. *Chem. Mater.* **2017**, *29*, 3854−3857.
(64) Al-Shakban, M.; Matthews, P. D.; Deogratias, G.; McNaughter, P. D.; Raftery, J.; Vitorica-Yrezabal, I.; Mubofu, E. B.; O'Brien, P. Novel Xanthate Complexes for the Size-Controlled Synthesis of Copper Sulfide Nanorods. *Inorg. Chem.* **2017**, *56*, 9247−9254.
(65) Zhai, Y.; Shim, M. Effects of Copper Precursor Reactivity on the Shape and Phase of Copper Sulfide Nanocrystals. *Chem. Mater.* **2017**, *29*, 2390−2397.
(66) van Oversteeg, C. H. M.; Oropeza, F. E.; Hofmann, J. P.; Hensen, E. J. M.; de Jongh, P. E.; de Mello Donega, C. Water-Dispersible Copper Sulfide Nanocrystals *via* Ligand Exchange of 1-Dodecanethiol. *Chem. Mater.* **2019**, *31*, 541−552.
(67) Tang, A.; Qu, S.; Li, K.; Hou, Y.; Teng, F.; Cao, J.; Wang, Y.; Wang, Z. One-Pot Synthesis and Self-Assembly of Colloidal Copper(I) Sulfide Nanocrystals. *Nanotechnology* **2010**, *21*, 285602.
(68) Liu, L.; Zhong, H.; Bai, Z.; Zhang, T.; Fu, W.; Shi, L.; Xie, H.; Deng, L.; Zou, B. Controllable Transformation from Rhombohedral $Cu_{1.8}S$ Nanocrystals to Hexagonal CuS Clusters: Phase- and Composition-Dependent Plasmonic Properties. *Chem. Mater.* **2013**, *25*, 4828−4834.
(69) Nelson, A.; Ha, D.-H.; Robinson, R. D. Selective Etching of Copper Sulfide Nanoparticles and Heterostructures through Sulfur Abstraction: Phase Transformations and Optical Properties. *Chem. Mater.* **2016**, *28*, 8530−8541.
(70) Liu, Y.; Liu, M.; Swihart, M. T. Reversible Crystal Phase Interconversion between Covellite CuS and High Chalcocite Cu_2S Nanocrystals. *Chem. Mater.* **2017**, *29*, 4783−4791.
(71) Sigman, M. B.; Ghezelbash, A.; Hanrath, T.; Saunders, A. E.; Lee, F.; Korgel, B. A. Solventless Synthesis of Monodisperse Cu_2S Nanorods, Nanodisks, and Nanoplatelets. *J. Am. Chem. Soc.* **2003**, *125*, 16050−16057.
(72) van der Stam, W.; Akkerman, Q. A.; Ke, X.; van Huis, M. A.; Bals, S.; de Mello Donega, C. Solution-Processable Ultrathin Size- and Shape-Controlled Colloidal $Cu_{2-x}S$ Nanosheets. *Chem. Mater.* **2015**, *27*, 283−291.
(73) van der Stam, W.; Rabouw, F. T.; Geuchies, J. J.; Berends, A. C.; Hinterding, S. O. M.; Geitenbeek, R. G.; van der Lit, J.; Prévost, S.; Petukhov, A. V.; de Mello Donega, C. *In Situ* Probing of Stack-Templated Growth of Ultrathin $Cu_{2-x}S$ Nanosheets. *Chem. Mater.* **2016**, *28*, 6381−6389.
(74) van der Stam, W.; Gradmann, S.; Altantzis, T.; Ke, X.; Baldus, M.; Bals, S.; de Mello Donega, C. Shape Control of Colloidal $Cu_{2-x}S$ Polyhedral Nanocrystals by Tuning the Nucleation Rates. *Chem. Mater.* **2016**, *28*, 6705−6715.
(75) Wang, L.-W. High Chalcocite Cu_2S: A Solid-Liquid Hybrid Phase. *Phys. Rev. Lett.* **2012**, *108*, 085703.
(76) Rivest, J. B.; Fong, L.-K.; Jain, P. K.; Toney, M. F.; Alivisatos, A. P. Size Dependence of a Temperature-Induced Solid−Solid Phase Transition in Copper(I) Sulfide. *J. Phys. Chem. Lett.* **2011**, *2*, 2402−2406.

https://doi.org/10.1021/acsnano.1c01488
ACS Nano 2021, 15, 9987−9999

(77) Chakrabarti, D. J.; Laughlin, D. E. The Cu-S (Copper-Sulfur) System. *Bull. Alloy Phase Diagrams* **1983**, *4*, 254−271.
(78) Horani, F.; Lifshitz, E. Unraveling the Growth Mechanism Forming Stable γ-In_2S_3 and β-In_2S_3 Colloidal Nanoplatelets. *Chem. Mater.* **2019**, *31*, 1784−1793.
(79) Pearson, R. G. Absolute Electronegativity and Hardness: Application to Inorganic Chemistry. *Inorg. Chem.* **1988**, *27*, 734−740.
(80) White, S. L.; Smith, J. G.; Behl, M.; Jain, P. K. Co-Operativity in A Nanocrystalline Solid-State Transition. *Nat. Commun.* **2013**, *4*, 2933.
(81) Routzahn, A. L.; Jain, P. K. Single-Nanocrystal Reaction Trajectories Reveal Sharp Cooperative Transitions. *Nano Lett.* **2014**, *14*, 987−992.

https://doi.org/10.1021/acsnano.1c01488
ACS Nano 2021, 15, 9987−9999